J. Fluid Mech. (2004), *vol.* 518, *pp.* 187–214. © 2004 Cambridge University Press
DOI: 10.1017/S0022112004001041 Printed in the United Kingdom

Choked flows in open capillary channels: theory, experiment and computations

By UWE ROSENDAHL, ANTJE OHLHOFF AND MICHAEL E. DREYER†

Center of Applied Space Technology and Microgravity (ZARM), University of Bremen, Am Fallturm, Bremen, D-28359, Germany

(Received 14 May 2003 and in revised form 22 June 2004)

This paper is concerned with flow-rate limitations in open capillary channels under low-gravity conditions. The channels consist of two parallel plates bounded by free liquid surfaces along the open sides. In the case of steady flow the capillary pressure of the free surface balances the differential pressure between the liquid and the surrounding constant-pressure gas phase. A maximum flow rate is achieved when the adjusted volumetric flow rate exceeds a certain limit leading to a collapse of the free surfaces.

In this study the steady one-dimensional momentum equation is solved numerically for perfectly wetting incompressible liquids to determine important characteristics of the flow, such as the free-surface shape and limiting volumetric flow rate. Using the ratio of the mean liquid velocity and the longitudinal small-amplitude wave speed a local capillary speed index S_{ca} is introduced. A reformulation of the momentum equation in terms of this speed index illustrates that the volumetric flow rate is limited. The maximum flow rate is reached if $S_{ca} = 1$ locally, a phenomenon called choking in compressible flows. Experiments with perfectly wetting liquids in the low-gravity environment of a drop tower and aboard a sounding rocket are presented where the flow rate is increased in a quasi-steady manner up to the maximum value. The experimental results are in very good agreement with the numerical predictions. Furthermore, the influence of the S_{ca} on the flow-rate limit is confirmed.

1. Introduction

The phenomenon of flow-rate limitation caused by a choked flow is well-known from one-dimensional flows in gas dynamics and liquid flows in open channels under terrestrial conditions. Choking occurs when the fluid velocity v locally reaches a limiting wave speed. In compressible gas duct flows, the characteristic limiting wave speed is defined by the speed of sound v_s. The characteristic number is the Mach number ($Ma \equiv v/v_s$), and the maximum flow passes through a duct when $Ma = 1$. In gravity dominated open channel flows, the speed of shallow-water waves v_{sw} corresponds to the limiting velocity. The flow is characterized by the Froude number ($Fr \equiv v/v_{sw}$), and choking occurs for $Fr = 1$. A close analogy exists between both flow types since the pressure-induced variation of density influences the gas flow in the same manner as the pressure-induced change of cross-sectional area influences the open-channel flow. As a consequence, the specific characteristic wave speeds can be derived from the same universal form. The velocities given above are defined in table 2.

† Author to whom correspondence should be addressed: dreyer@zarm.uni-bremen.de

https://doi.org/10.1017/S0022112004001041 Published online by Cambridge University Press

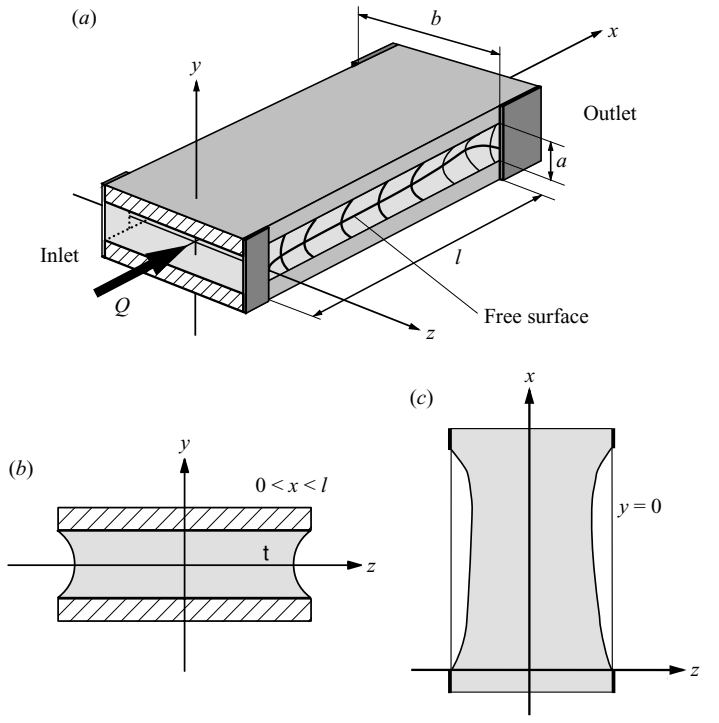


FIGURE 1. (*a*) Liquid flow through an open capillary channel consisting of two parallel plates. The free surfaces along the flow path x bend inwards. (*b*) Cross-sectional area for $x = const.$ (*c*) The symmetry plane $y = 0$.

In our investigation, we found that a similar phenomenon occurs if liquid flows through an open capillary channel, as depicted in figure 1(*a*), leading to a limitation in flow rate Q in the steady case. The channel consists of two parallel plates that are connected to ducts of closed circumference. For an internal pressure p lower than ambient pressure p_a, the free liquid surfaces are concave at any cross-section, as shown in figure 1(*b*). The pressure decreases in the flow direction, thus the curvatures of the surfaces increase and the flow path constricts as indicated in 1(*c*). A steady flow is obtained only for a flow rate below a critical value ($Q < Q_{crit}$). For $Q > Q_{crit}$, the liquid surfaces collapse at the channel outlet and the flow changes from steady single-phase flow to unsteady two-phase flow. Analogous to these phenomena, we introduce the capillary speed index $S_{ca} \equiv v/v_{ca}$ where v_{ca} is the speed of longitudinal small-amplitude waves in open capillary channels. The theoretical considerations, as well as the experiments and the numerical computations, show that the flow limit is reached for $S_{ca} = 1$.

Open capillary channels are used in a number of applications in space liquid management, i.e. heat pipes and propellant management devices (PMD) in surface tension tanks of satellites. Concerning the latter, open channels are often used for the transport and positioning of propellants. However, in spite of the high number of applications the effect of flow-rate limitation in open capillary flows is not well understood, requiring greater design margins or redundancy. Few publications that study a forced liquid flow through open capillary channels consider the limiting

https://doi.org/10.1017/S0022112004001041 Published online by Cambridge University Press

Lengths	Velocities	Others	Characteristic numbers
$x = x'/l$	$v_c = \sqrt{2\sigma/(\rho' a)}$	$A_0 = ab$	$Oh = \sqrt{\rho' v^2/(2\sigma a)}$
$y = 2y'/a$	$v = v'/v_c$	$A = A'/A_0$	$\Lambda = b/a$
$z = 2z'/a$	$v_{ca} = v'_{ca}/v_c$	$Q = Q'/(A_0 v_c)$	$\tilde{l} = Oh\, l/(4a)$
$k = 2k'/a$		$p = ap'/(2\sigma)$	
$R = 2R'/a$		$\Gamma = a/(2l)$	
$R_{1,2} = 2R'_{1,2}/a$		$S_{ca} = v/v_{ca}$	
$h = ah'/2$		$Re = 2av'/\nu$	

TABLE 1. Non-dimensional variables and characteristic numbers.

flow rates. Jaekle (1991) performed numerical computations of a liquid flow in a T-shaped capillary channel. Neglecting the surface curvature in the flow direction, the one-dimensional momentum equation was solved numerically yielding the radius of curvature in the cross-sectional plane and corresponding flow rates of steady and time-dependent flows. For this model, solutions for interface shapes could not be computed for all flow rates. Jaekle attributes this phenomenon to choking, without going into details. Experimental investigations of forced flow through an open capillary parallel-plate channel were performed in a 4.74 s drop tower by Rosendahl *et al.* (2002). An upper bound was found for the steady volumetric flow rate. Above that limit, the free surfaces collapsed and gas ingestion occurred at the channel outlet. The experiments are based on the work of Dreyer, Delgado & Rath (1994). They investigated the rise of liquid between two parallel plates after a step reduction of gravity in a drop tower. It was shown that the velocity of the rising liquid cannot exceed $v_c\sqrt{1-\Lambda^{-1}}$, a critical velocity similar to that introduced in the present work. Here, v_c is the characteristic velocity defined in table 1 and $\Lambda = b/a$ is the aspect ratio of the channel. Likewise, motivated by challenges in low-gravity propellant management, Srinivasan (2003) computed the flow rates of capillary self-driven liquid flows in open parallel-plate channels. A semi-analytical method for the solution of the steady three-dimensional Stokes equations was proposed that assumes extremely small flow rates. For two data sets, the computations were compared to the experimental results from Rosendahl *et al.* (2002). The computed flow rate was approximately three times lower than the experimental measurement which the author attributes to the inertia in the experiment.

In summary, we found a flow limitation in open capillary channels which is similar to choking in compressible duct flows and open channel flows under gravity. Our experimental, numerical and analytical results coincide well and demonstrate the general features of choked capillary channel flows.

This paper is organized in six sections. In § 2, the flow through the open capillary channel is formulated. Attention is drawn to the modelling of the free surface and the irreversible pressure loss along the flow path. The numerical procedure used to solve the governing equations is also introduced. In analogy to similar flows, § 3 identifies the effect of the flow-rate limitation for open capillary channels. The experimental set-ups and procedures are presented in § 4, and in § 5 the experimental, numerical and analytical results are compared. Characteristic features of the flow such as contour lines of the surface profiles and maximum flow rate are discussed as well as the influence of S_{ca}. The paper is summarized in § 6.

https://doi.org/10.1017/S0022112004001041 Published online by Cambridge University Press

2. The model

The flow of an incompressible Newtonian liquid through an open parallel-plate channel, as shown in figure 1(*a*), is considered. The gap distance, the width of the plates and the length of the open section are denoted by a, b and l, respectively. The origin of the coordinate system is located in the centre of the inlet cross-section. Since all experiments were performed with perfectly wetting liquids, the model is restricted to this case. Isothermal conditions are assumed. The model is restricted to steady flow conditions for $Q < Q_{crit}$, thus the process of the collapsing surfaces is not considered. Since the maximum Reynolds number $Re < 10^3$ (see table 1), the flow is considered to remain laminar.

2.1. *Scaling*

The flow along the channel axis x is assumed to be one-dimensional (see § 2.5) and is characterized by the mean velocity v and the liquid pressure p. Table 1 provides the quantities used for non-dimensionalization. Velocities are scaled by $v_c = \sqrt{2\sigma/(\rho' a)}$ where σ is the surface tension and ρ' the density (the prime is necessary here to distinguish the constant dimensional density from the variable non-dimensional density used in § 3). The cross-sectional area A is scaled by $A_0 = ab$. The x-axis is scaled with the channel length l, all other lengths with $a/2$. For the discussion of the physical effects, the dimensionless length $\tilde{l}$

$$\tilde{l} = \frac{Ohl}{4a} \tag{2.1}$$

is preferred, which is the usual scaling of frictional duct flows. Here, Oh is the Ohnesorge number

$$Oh = \sqrt{\frac{\rho' \nu^2}{2\sigma a}} = \frac{2}{Re_c} \text{ where } Re_c = \frac{2a v_c}{\nu}, \tag{2.2}$$

where ν denotes the kinematic viscosity. Note that Oh is inversely proportional to the Reynolds number, based on the characteristic velocity v_c. The third characteristic number is the aspect ratio $\Lambda = b/a$.

The Bond numbers

$$Bo_i = \frac{\rho' g_i a L_i}{2\sigma}, \tag{2.3}$$

which are obtained for each axis $i = x, y, z$ with the characteristic length $L_i = a, b, l$, respectively, are defined by the ratio of the hydrostatic pressure caused by the acceleration g_i and the capillary pressure. Since all experiments are performed under reduced gravity conditions (see § 4), Bo_i is always $O(10^{-3})$ and therefore the effect of the hydrostatic pressure is not considered.

2.2. *Governing equations*

The dimensionless governing equations are the momentum equation in flow direction x

$$\mathrm{d}p + v\,\mathrm{d}v - \mathrm{d}w_f = 0 \tag{2.4}$$

and the mass balance equation

$$\frac{\mathrm{d}A}{A} + \frac{\mathrm{d}v}{v} = \frac{\mathrm{d}Q}{Q} = 0, \tag{2.5}$$

where $\mathrm{d}w_f$ is the local irreversible pressure loss per unit volume. The volumetric flow rate Q is defined by $Q = Av$. The capillary pressure $p - p_a$ is related to the

https://doi.org/10.1017/S0022112004001041 Published online by Cambridge University Press

curvature of the free surface by the Gauss–Laplace equation (assuming zero normal and tangential stresses at the free surface and a passive overlying gas)

$$p - p_a = -h = -\left(\frac{1}{R_1} + \frac{1}{R_2}\right) \tag{2.6}$$

(Landau & Lifschitz 1959), where $h/2$ is the mean curvature of the liquid surface. R_1 and R_2 are the principal radii of curvature to be considered in § 2.3. Since the ambient pressure p_a is constant, the pressure gradient in (2.4) becomes

$$\mathrm{d}p = -\mathrm{d}h. \tag{2.7}$$

Applying (2.5), the convective term of (2.4) can be rewritten as

$$v\,\mathrm{d}v = -\frac{Q^2}{A^3}\,\mathrm{d}A. \tag{2.8}$$

The irreversible pressure loss due to viscous forces $\mathrm{d}w_f$ consists of two parts, the fully developed laminar viscous pressure loss $\mathrm{d}w_{pf}$ and an additional entrance pressure loss $\mathrm{d}w_{Sf}$ which is a result of the change of the velocity profile from the entrance profile to the parabolic velocity distribution (Poiseuille flow). The modelling of this additional pressure loss is important for reproducing the experimental results. For one-dimensional flows with constant cross-section, both pressure losses can be derived from analytical solutions of the Navier–Stokes equation. The local pressure loss of a fully developed flow reads

$$\mathrm{d}w_{pf} = -\frac{K_{pf}Oh}{8a} l v\,\mathrm{d}x = -\frac{K_{pf}}{2}\tilde{l} v\,\mathrm{d}x, \tag{2.9}$$

with $K_{pf} = 96$ (White 1986). For the additional pressure loss due to the profile change, a solution deduced by Sparrow & Lin (1964) is applied. Only the conclusion is presented here. Assuming an initial plug flow in the entrance cross-section, the additional total pressure loss $\Delta p'$ is given by $\Delta p'/(\rho'/2v'^2) = K_{Sf}(\hat{x})$, where K_{Sf} is the local loss factor depending on the coordinate $\hat{x} = 4\nu x'/(a^2 v')$. The differential form yields

$$\mathrm{d}w_{Sf} = -8\hat{K}_{Sf}(x)\tilde{l} v\,\mathrm{d}x \text{ where } \hat{K}_{Sf} = \frac{\mathrm{d}K_{Sf}(\hat{x})}{\mathrm{d}\hat{x}}. \tag{2.10}$$

Note that this term only contributes within the entrance length l_e in which the profile changes proceed. In the experimental configuration, the flow passes a duct before entering the open channel. Therefore, the velocity profile at the channel inlet is partly developed and deviates from the assumed plug profile. To consider this entrance velocity profile, the coordinate x in (2.10) is shifted by a parameter s_0. For $s_0 = 0$, the inlet velocity distribution is constant and the integration of $\mathrm{d}w_{Sf}$ along the complete entrance length is required. For $s_0 \geqslant l_e$, the parabolic profile is fully developed, thus $\mathrm{d}w_{Sf} = 0$. In the experimental part, s_0 is provided based on three-dimensional numerical calculation of the flow path before the channel entrance. Finally, the total irreversible pressure loss $\mathrm{d}w_f$ is determined by

$$\mathrm{d}w_f = -0.5[K_{pf} + 16\hat{K}_{Sf}(x + s_0)]\tilde{l} v\,\mathrm{d}x. \tag{2.11}$$

2.3. *Modelling of the free liquid surface*

To solve (2.4) and (2.5), an additional relation is required that connects the cross-sectional area A to the capillary pressure p or mean curvature $h/2$. Because of the low Bond number, the free surfaces are symmetric with respect to the planes $y = 0$

https://doi.org/10.1017/S0022112004001041 Published online by Cambridge University Press

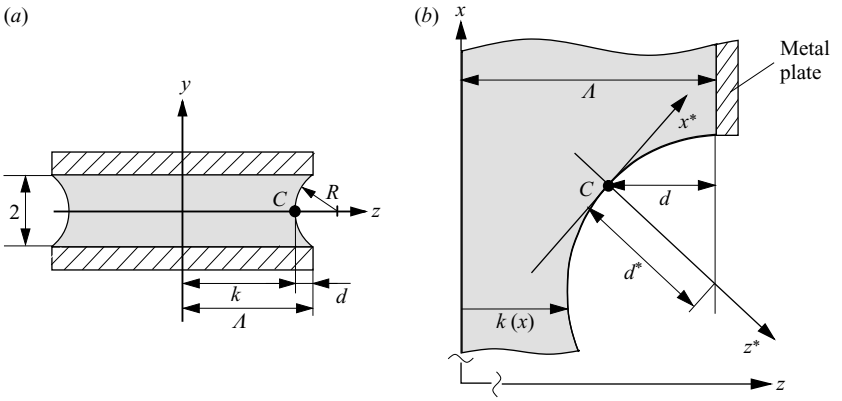


FIGURE 2. (*a*) Cross-section of the channel in the (y, z)-plane at constant x. (*b*) Section through the liquid in the (x, z)-plane at $y = 0$.

and $z = 0$ and the following considerations are restricted to the surface position k in the symmetry plane $y = 0$

$$k(x) = z(x, y = 0) \tag{2.12}$$

with $k(x) \geqslant 0$. As shown in figure 2(*a*), k defines the innermost line (the profile) of the free-surface shape which is easily identified in experiments and serves well for a comparison between experiments and theory. The aim of this section is to define h and A as a function of k and its derivatives with respect to x, $\mathrm{d}_x k = \mathrm{d}k/\mathrm{d}x$ and $\mathrm{d}_{xx} k = \mathrm{d}^2 k/\mathrm{d}x^2$. Since k defines the minimum surface position (see figure 2*a*), the first derivative in the y-direction vanishes at $y = 0$ and the general form of the mean surface curvature (Bronstein & Semendjajew 2004) reduces to

$$h(x, y = 0) = \frac{1}{R_1} + \frac{1}{R_2} = \frac{1}{R_1} + \frac{\Gamma^2 \mathrm{d}_{xx} k}{[1 + \Gamma^2 (\mathrm{d}_x k)^2]^{3/2}} \text{ where } \Gamma = a/(2l). \tag{2.13}$$

The second term on the right-hand side defines the component of the surface curvature in the (x, z)-plane at $y = 0$ given by the reciprocal principal radius of curvature R_2 (radius in flow direction). The first term is the component of curvature in the (y, z^*)-plane, which is given by the reciprocal principal radius of curvature R_1 perpendicularly to R_2. Referring to figure 2(*b*), the axis z^* is normal to the profile line k located at an arbitrary point $C(x, y = 0, z)$ and the planes (x, z) and (y, z^*) are the corresponding principal normal planes. We assume, that the pressure in the principal plane (y, z^*) is constant in the vicinity of the free surface. Then, the curvature in this plane is constant and the surface is a segment of a circle with radius R_1 that may be derived using the geometrical relations of figure 3(*a*), namely

$$R_1 = \frac{1 + d^{*2}}{2d^*}, \qquad d^* = d[1 + \Gamma^2 (d_x k)^2]^{1/2}, \qquad d = \Lambda - k. \tag{2.14}$$

Equation (2.14) holds for $d^* \leqslant 1$, which means that the liquid is pinned at the edges of the channel and R_1 may change between infinity (plane surface) and $R_1 = 1$ (maximum curvature). Thus $k \geqslant \Lambda - [1 + \Gamma^2 (\mathrm{d}_x k)^2]^{-1/2}$. In some experiments, a second configuration can be observed in which the liquid separates from the edges of the channels, as shown in figure 3(*b*). The free surface moves inwards between the parallel plates and the cross-sectional area decreases further. This separation typically occurs for large values of $\tilde{l}$ at the outlet. Since the contact angle between the liquid and

https://doi.org/10.1017/S0022112004001041 Published online by Cambridge University Press

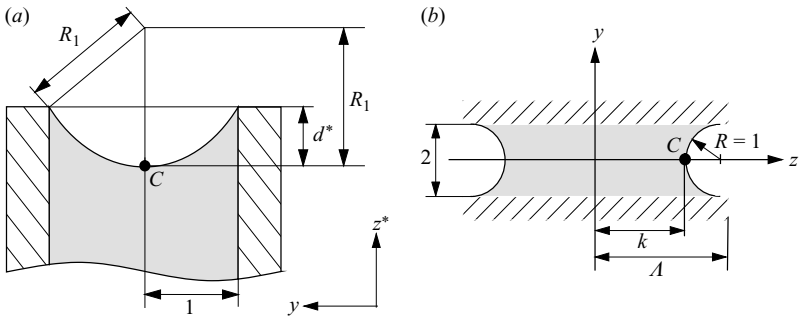


FIGURE 3. (*a*) Section through the liquid at the (y, z^*)-plane at the point C. (*b*) Cross-section of the channel in the (y, z)-plane at constant x for the case where the free surface is detached from the edge.

the solid is zero (perfectly wetting liquid are used), the radius of curvature is half the distance between the plates, $R_1 = 1$. In summary, both pinned and separated conditions are given by

$$R_1 = \begin{cases} \dfrac{1+(\Lambda-k)^2[1+\Gamma^2(\mathrm{d}_x k)^2]}{2(\Lambda-k)[1+\Gamma^2(\mathrm{d}_x k)^2]^{1/2}} & \text{for} \quad k \geqslant \Lambda - [1+\Gamma^2(\mathrm{d}_x k)^2]^{-1/2}, \\ 1 & \text{for} \quad k < \Lambda - [1+\Gamma^2(\mathrm{d}_x k)^2]^{-1/2}. \end{cases} \tag{2.15}$$

By applying (2.15) to (2.13), the capillary pressure is given by k and its derivatives with respect to x, $h = h(k, \mathrm{d}_x k, \mathrm{d}_{xx} k)$. For the calculation of the cross-sectional area A (see figures 2*a* and 3*b*), we assume a rectangle minus two segments of a circle with radius R in the (y, z)-plane. Then we obtain

$$A(k) = \begin{cases} 1 - \dfrac{R^2}{2\Lambda}\arcsin\dfrac{1}{R} + \dfrac{1}{2\Lambda}(R - \Lambda + k) \text{ where } R = \dfrac{1+(\Lambda-k)^2}{2(\Lambda-k)} & \text{for} \quad k \geqslant \Lambda - 1, \\ (k + 1 - \pi/4)/\Lambda & \text{for} \quad k < \Lambda - 1. \end{cases} \tag{2.16}$$

Note, that A is a function of the profile line k only. For small changes of $k(x)$, the principal radius of curvature R_1 is approximately the same as the radius R in the coordinate plane.

2.4. *Final equations*

Substituting the capillary pressure (2.7), the convective term (2.8) and flow losses (2.11) into the governing equations (2.4), (2.5) yields

$$\mathrm{d}_x h + \frac{Q^2}{A^3}\,\mathrm{d}_k A\,\mathrm{d}_x k - [K_{pf} + 16\hat{K}_{Sf}(x + s_0)]\frac{Q\tilde{l}}{2A} = 0 \tag{2.17}$$

and

$$\Gamma^2\,\mathrm{d}_{xx} k + \left(\frac{1}{R_1} - h\right)[1+\Gamma^2(\mathrm{d}_x k)^2]^{3/2} = 0, \tag{2.18}$$

respectively. The boundary conditions are the position of the liquid surface at the channel inlet and outlet (the surface is pinned at the edges of the closed ducts) and the surface curvature at the inlet:

$$\begin{aligned} k(x=0) &= k(x=1) = \Lambda, \\ h(x=0) &= h_0. \end{aligned} \tag{2.19}$$

https://doi.org/10.1017/S0022112004001041 Published online by Cambridge University Press

The values for h_0 and s_0 will be computed numerically for the special experimental configuration (see § 4.4). Note that in the experimental configuration, $k(x=0)$ and $k(x=1)$ are not exactly equal to Λ. Therefore, in our numerical algorithm we use the exact boundary condition to be consistent with the experiments.

2.5. *Principal assumptions and limitations of the model*

In this section, we justify our principal assumption: the flow along the channel axis x is one-dimensional, which requires (i) that the velocity component in the flow direction is considerably greater than the lateral flow components and (ii) that the rate of change of the cross-section in the flow direction is sufficiently small. The first requirement depends on the experiment design and is approximated well in the case of the sounding rocket experiment as discussed in § 4.4. The second requirement is fulfilled well for the main flow path. Deviations from these conditions are to be expected at the channel inlet and outlet and are discussed in § 5.2. To comply with these assumptions, we limit the validity of our work to $\Lambda \geqslant 3$.

Because of the low-gravity environment, the hydrostatic pressure distribution over the channel cross-section is negligible, and $\partial p/\partial y, \partial p/\partial z \ll \partial p/\partial x$ follows from the momentum equation. Thus, the pressure p over the flow cross-section area A may be considered as constant. Deviating from this assumption, the surface modelling assumes a constant pressure in the main curvature plane, which is more realistic for the inlet and outlet region.

For the parallel-plate flow with $A = const$, analytical solutions are known, providing the distribution of the velocity and the pressure along the channel axis x (see § 2.2). According to the usual methods for quasi one-dimensional flows, the pressure distribution gained from the constant cross-section problem is applied locally.

2.6. *Numerical procedure*

For the numerical solution of the coupled nonlinear system (2.17)–(2.19), we treat h and k as variables and use finite differences. For the short and medium channels, we use a uniform grid with $N \geqslant 200$ discrete points. To limit computation time, we use adaptive grids for the long channels, employing smaller grid spaces in the vicinity of the strongest necking and wider grid spaces elsewhere with $N = 800$ points. In the inner region, the derivatives $\mathrm{d}_x k$ and $\mathrm{d}_{xx} k$ are discretized by second-order central differences and, for a better stability, $\mathrm{d}_x h$ is discretized by a first-order backward difference. At the outlet boundary point, the derivative $\mathrm{d}_x k$ in (2.17) is calculated by a first-order backward difference. The system of nonlinear equations is solved with the classical Newton method and yields the position $k(x) = f(Oh, \Lambda, \tilde{l}, Q)$ of the liquid surface as well as the velocity $v(x)$ and the curvature $h(x)$ with the same dependence.

As the numerical critical flow rate Q_{crit}^{num}, we define the maximum flow rate Q leading to the convergence of the numerical algorithm (with a relative error of 10^{-7} and a maximum of 25 Newton iterations). For the numerical computations of the speed index at the smallest cross-section, this point is computed using a Neville interpolation from the three nearest points (Press *et al.* 1992). For the speed index itself (see (3.3)), we use a second-order central difference on three adjacent flow rates, namely

$$S_{ca}^{num}(Q_2, x) = \frac{Q_2}{A(Q_2, x)} \left[-A(Q_2, x) \frac{h(Q_3, x) - h(Q_1, x)}{A(Q_3, x) - A(Q_1, x)} \right]^{-1/2} \tag{2.20}$$

with $Q_1 < Q_2 < Q_3$.

https://doi.org/10.1017/S0022112004001041 Published online by Cambridge University Press

	Compressible gas flow	Open channel flow		Elastic tube flow
		$Bo \gg 1$	$Bo \ll 1$	
Longitudinal wave speed	$v_s = \sqrt{\dfrac{\mathrm{d}p}{\mathrm{d}\hat{\rho}}}$	$v_{sw} = \dfrac{\sqrt{g_z k'}}{v_c}$	$v_{ca} = \sqrt{-A\dfrac{\mathrm{d}h}{\mathrm{d}A}}$	$v_e = \sqrt{A\dfrac{\mathrm{d}(p-p_a)}{\mathrm{d}A}}$
Dimensionless number	$Ma = v/v_s$	$Fr = v/v_{sw}$	$S_{ca} = v/v_{ca}$	$S = v/v_e$

TABLE 2. Overview of the dimensionless numbers derived from the general longitudinal wave speed (3.1).

3. The effect of flow-rate limitation

In many ways, one-dimensional steady flows such as in open channels, in flexible tubes and compressible gas flows are similar since the governing equations of these flows are derived from the same conservation equations of mass and momentum. For such flows, the mass flow rate is limited owing to a choking effect. The key role is played by the longitudinal small-amplitude wave speed

$$c = \sqrt{A\frac{\mathrm{d}p}{\mathrm{d}(\hat{\rho}A)}}, \tag{3.1}$$

which is based on the assumption that the cross-section area A as well as the density $\hat{\rho}$ (scaled with ρ') varies with the liquid pressure only (see Lighthill 1978). The maximum flow rate is reached when the flow locally achieves c.

For particular flows, (3.1) simplifies. Some special cases are given in table 2. For compressible flows with constant cross-sectional area, $A = const$, (3.1) yields the speed of sound at constant entropy which defines the Mach number Ma. For open-channel flows under normal gravity ($Bo \gg 1$) with variable cross-section of the flow path and constant density, (3.1) yields the shallow-water wave speed which defines the Froude number Fr. The wave speed in a flexible tube depends on the relation between the cross-section and the differential pressure across the tube wall, $p - p_a$ (Shapiro 1977). The characteristic number is the speed index S which approaches unity in the case of choking similarly as does Ma and Fr. The work of Shapiro (1953) is recommended owing to its description of choking phenomena and detailed derivation of all relevant equations.

For the case of capillary flows ($Bo \ll 1$ and $\hat{\rho} = \rho = 1$), we generalize the wave speed of Jaekle (1991) to obtain

$$v_{ca} = \sqrt{-A\frac{\mathrm{d}h}{\mathrm{d}A}}, \tag{3.2}$$

after substituting the pressure in (3.1) by $p_a - h$ from (2.6). Scaling the mean liquid velocity $v = Q/A$ by (3.2) yields the capillary speed index

$$S_{ca} = \frac{v'}{v'_{ca}} = \frac{v}{v_{ca}} = Q\sqrt{-\frac{\mathrm{d}A}{A^3\mathrm{d}h}}. \tag{3.3}$$

Note that for the calculation of (3.2), a one-to-one relation between the capillary pressure and the cross-section $A = A(h)$ is required, which is unknown in general.

Owing to the similarities of the flow highlighted in table 2, the flow rate of an open capillary channel flow reaches its maximum when $S_{ca} = 1$ somewhere along the channel, as will be shown using a simplified model. From the integration of (2.4) it

https://doi.org/10.1017/S0022112004001041 Published online by Cambridge University Press

follows that the total pressure P, defined by

$$P = p + \tfrac{1}{2}v^2 = p_a - h + \tfrac{1}{2}v^2, \tag{3.4}$$

varies along the channel axis x because of the influence of friction. We assume, that P is constant at an arbitrary but fixed position of the channel. With (3.4), the volumetric flow rate may be written as

$$Q = Av = A\sqrt{2(P - p_a + h)}. \tag{3.5}$$

The maximum flow rate is reached if the derivative of Q with respect to h vanishes. After simplification of (3.5) by means of (3.2) and the definition of S_{ca} we obtain

$$\frac{\mathrm{d}Q}{\mathrm{d}h} = \frac{A}{v}\left(1 - S_{ca}^2\right). \tag{3.6}$$

Thus, the flow rate is maximal for $S_{ca} = 1$. In keeping with the choked-flow analogy, we denote a flow with $S_{ca} < 1$ as subcritical. The case $S_{ca} > 1$ is not considered in this paper.

To further demonstrate the 'choking effect' in our flow problem, a reformulation of (2.17) is required. For this reason, the dependent variables p (or h), A and S_{ca} are formulated in terms of the independent variable x. Since $A = A(h)$, the differential relationship between $\mathrm{d}h$ and $\mathrm{d}A$ is given by

$$\frac{\mathrm{d}A}{A} = \frac{1}{A}\frac{\mathrm{d}A}{\mathrm{d}h}\mathrm{d}h = -\frac{\mathrm{d}h}{v_{ca}^2} = -\frac{S_{ca}^2}{v^2}\,\mathrm{d}h. \tag{3.7}$$

Differentiation of (3.2) yields

$$2\frac{\mathrm{d}v_{ca}}{v_{ca}} = M\frac{\mathrm{d}A}{A} \text{ where } M = 1 + A\frac{\mathrm{d}^2h/\mathrm{d}A^2}{\mathrm{d}h/\mathrm{d}A}. \tag{3.8}$$

Under application of (2.5) and (3.8), differentiation of the square of (3.3) yields

$$\frac{\mathrm{d}S_{ca}^2}{S_{ca}^2} = 2\frac{\mathrm{d}v}{v} - 2\frac{\mathrm{d}v_{ca}}{v_{ca}} = -2\frac{\mathrm{d}A}{A} - 2\frac{\mathrm{d}v_{ca}}{v_{ca}} = -(2 + M)\frac{\mathrm{d}A}{A}. \tag{3.9}$$

The following relations are obtained by straightforward algebraic manipulation. Substituting (3.7) into (2.17), the change of the capillary pressure in flow direction becomes

$$\mathrm{d}h = \frac{(K_{pf} + 16\hat{K}_{Sf})\tilde{l}Q}{2A\left(1 - S_{ca}^2\right)}\,\mathrm{d}x. \tag{3.10}$$

Applying (3.7) and (3.9) to (3.10) yields

$$\frac{\mathrm{d}S_{ca}^2}{S_{ca}^2} = (2 + M)\frac{S_{ca}^2A(K_{pf} + 16\hat{K}_{Sf})\tilde{l}}{2Q\left(1 - S_{ca}^2\right)}\,\mathrm{d}x = -(2 + M)\frac{\mathrm{d}A}{A}. \tag{3.11}$$

The equations (3.10) and (3.11) define the change of the dependent variables h, A and S_{ca} in flow direction x. Since M, K_{pf}, $\hat{K}_{Sf}$, $\tilde{l}$, A and Q are positive, the sign of (3.11) depends on the sign of $(1 - S_{ca}^2)$. For $S_{ca} < 1$, S_{ca} increases in flow direction and vice versa. The condition $S_{ca} = 1$ is a singular point where the derivative $\mathrm{d}S_{ca}/\mathrm{d}x$ is discontinuous. For a given Q and inlet speed index $S_{ca0} = S_{ca}(x = 0)$, (3.11) states that a maximum channel length l_{max} exists for which the $S_{ca}(x = l_{max}) = 1$. At this state it is impossible to increase l without changing the inlet boundary conditions. From (3.6) it follows that Q is maximal when $x = l_{max}$.

https://doi.org/10.1017/S0022112004001041 Published online by Cambridge University Press

Liquid	ρ' (kg m^{-3})	ν (10^{-6} m^2 s^{-1})	σ (N m^{-1})
PDMS	766 $\pm$ 0.2%	0.69 $\pm$ 2%	0.0158 $\pm$ 2%
FC-77	1773 $\pm$ 0.2%	0.85 $\pm$ 3%	0.0153 $\pm$ 3%

TABLE 3. Test liquids and properties at $T = 20\,^{\circ}$C. Polydimethylsiloxane (PDMS, silicone oil) provided by Dow Corning, Fluorinert liquid FC-77 provided by 3M. The static contact angle is $\gamma_{stat} = 0$ on Perspex and glass. The density, kinematic viscosity and surface tension are denoted by ρ', ν and σ, respectively.

4. Experiments

To verify the theoretical model presented in § 2, we performed experiments aboard a sounding rocket and in a drop tower. Both facilities provide a low-gravity environment of $g_i \sim 10^{-4} g_0$ and $g_i \sim 10^{-5} g_0$, respectively, satisfying $Bo \ll 1$ in all axes. The experiments performed in the 4.74 s drop tower in Bremen cover a wide range of the governing parameters Λ, Oh and $\tilde{l}$. The results show a good agreement with theoretical predictions concerning the contour profiles and the critical volumetric flow rates. However, because of the short experimental time, the expected influence of S_{ca} could not be observed clearly. An experiment with longer observation time was therefore developed for the sounding rocket TEXUS-37.† In contrast to the drop-tower experiments, the flow rate in the open capillary channel could be varied during the experiment period of 6 min allowing a stepwise increase to the limit of the steady flow. The following sections focus on the TEXUS-set-up, the performance and data evaluation. The drop-tower experiments are briefly summarized in § 4.2. Details are available from Rosendahl *et al.* (2002).

4.1. *Experiments aboard TEXUS-37*

4.1.1. *Experiment set-up*

A diagram of the experimental set-up is shown in figure 4. The core element of the set-up consists of a cylindrical liquid reservoir ② with a compensation tube ⑦ and an observation chamber ① with the open channel. The channel is connected to the liquid reservoir ② via a nozzle ③. The compensation tube as well as the nozzle can be closed pneumatically by a gate valve ⑧ and a stemple ④. The liquid reservoir was especially designed to enable a controlled filling of the channel at the beginning of the microgravity phase and provide defined boundary conditions at the channel inlet. The flow through the channel is established by two gear pumps. One pump (pu_1) supplies the reservoir through a circular gap on the bottom of the reservoir at flow rate Q_s. The flow enters through a screen-controlled rectifier ⑤ to ensure a homogenous velocity distribution. The second pump (pu_2) withdraws the liquid via the channel and the nozzle from the reservoir at flow rate Q. The unavoidable flow rate differences between both pumps are accommodated by the Perspex compensation tube ⑦ (inner diameter 45 mm).

The capillary channel consists of two parallel quartz plates with breadth $b = 25$ mm, gap $a = 5$ mm and length $l = 46.6$ mm. With the properties of the applied liquid polydimethylsiloxane (PDMS) from table 3, the governing parameters in table 4 are

† A video of the sounding rocket experiment aboard TEXUS-37 is available at http://www.zarm.uni-bremen.de/2forschung/grenzph/isoterm/crit_velo/chok_eng.htm.

https://doi.org/10.1017/S0022112004001041 Published online by Cambridge University Press

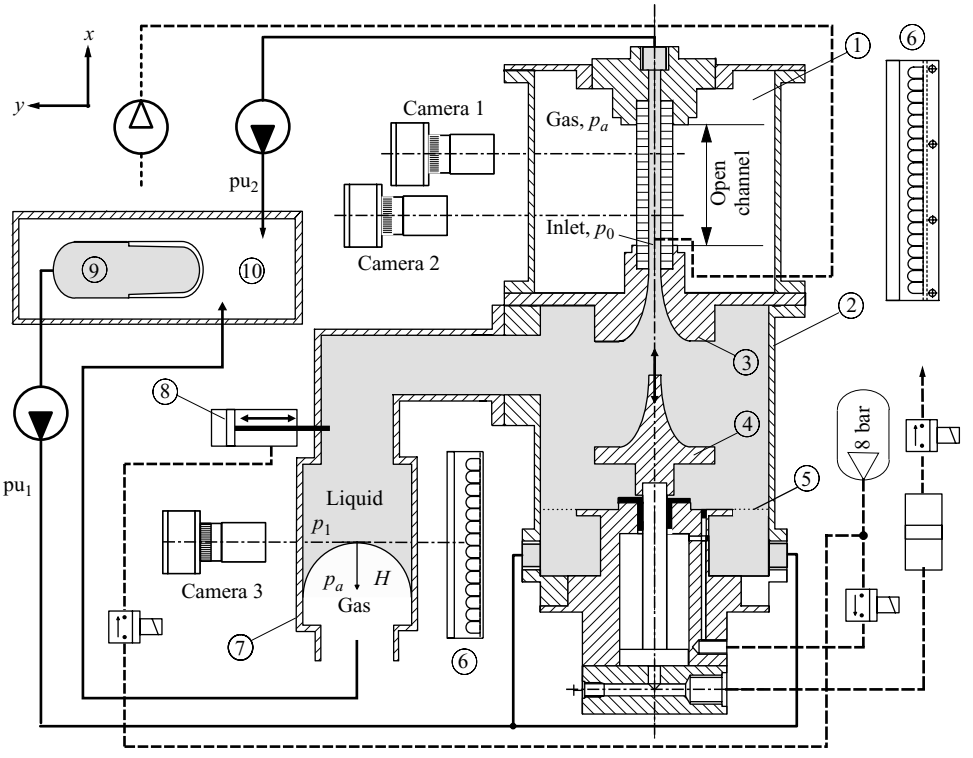


FIGURE 4. Diagram of the experimental set-up to investigate an open capillary channel flow aboard the sounding rocket TEXUS-37. The flow is established by the supply pump pu_1 and the withdrawal pump pu_2. ① observation chamber, ② liquid reservoir, ③ nozzle, ④ stemple, ⑤ screen, ⑥ illumination, ⑦ compensation tube, ⑧ gate valve, ⑨ supply membrane tank, ⑩ disposal tank. p_a is the ambient pressure, p_0 the pressure at the channel inlet, p_1 the pressure inside the compensation tube and H the position of the liquid meniscus.

Number	Liquid	a (mm)	b (mm)	l (mm)	t_r' (s)	Oh	Λ	$\tilde{l}$
TE-35a	PDMS	5	25	46.6	–	1.5×10^{-3}	5.0	3.5×10^{-3}
DT-29	FC-77	2	20	74.9	1.7	4.6×10^{-3}	10.0	4.3×10^{-2}
DT-32	PDMS	3	10	94.2	1.3	2.0×10^{-3}	3.3	1.5×10^{-2}
DT-33	PDMS	3	15	96.3	1.2	2.0×10^{-3}	5.0	1.6×10^{-2}
DT-34	PDMS	3	30	94.6	1.2	2.0×10^{-3}	10.0	1.5×10^{-2}
DT-35	PDMS	5	25	93.4	1.5	1.5×10^{-3}	5.0	7.1×10^{-3}
DT-35a	PDMS	5	25	48.4	0.7	1.5×10^{-3}	5.0	3.7×10^{-3}

TABLE 4. Experiment parameters for the experiments aboard of TEXUS-37 (TE) and in the drop tower (DT) with plate distance a, plate breath b, channel length l, rise time of the liquid meniscus t_r', Ohnesorge number Oh, aspect ratio Λ and dimensionless channel length $\tilde{l}$.

obtained (TE-35a). To prevent the spreading of liquid away from the channel, the inlet and outlet are covered by thin metal plates at the sides (① in figure 5*a*).

A front view normal to the plates is shown in figure 5(*a*). The channel has precise markings for the calibration and evaluation of the video images. Two CCD cameras were used. The camera fields of view overlap by approximately 10 mm, and the image

https://doi.org/10.1017/S0022112004001041 Published online by Cambridge University Press

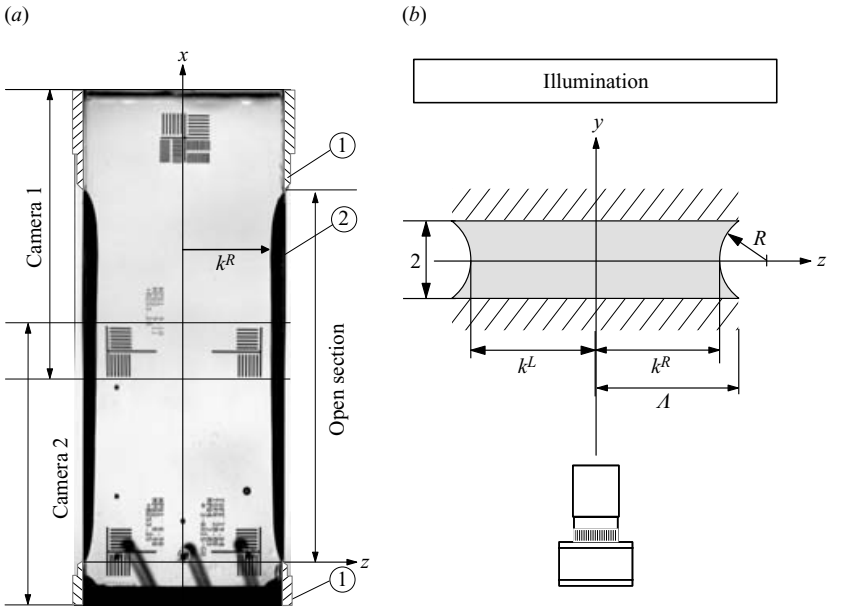


FIGURE 5. (*a*) Front view of the channel. The optical axes of the cameras are aligned normal to the top plate. The inlet and outlet are covered by thin FC-725 coated metal plates at the sides ①. Owing to total reflection, the liquid interfaces appear dark ②. (*b*) The profiles correspond to the distances k^L and k^R.

resolution is 47 μm/pixel. A homogeneous illumination is achieved by an LED panel with a Teflon diffusor (⑥ in figure 4). Owing to total reflection, the profiles of the gas–liquid interfaces appear as dark zones on the video images. Referring to figure 5(*b*), they are defined by the distances $\Lambda - k^L$ and $\Lambda - k^R$, where the positions $k^L(x)$ and $k^R(x)$ correspond to the left- and right-hand side profiles of the surface shape in the plane $y = 0$, respectively. During the experiment, the video signals were downlinked to the ground and recorded on VCR (S-VHS quality).

4.1.2. *Experiment performance*

The sounding rocket was launched from the ESRANGE (European Space Range), Kiruna, Sweden. During the ballistic flight phase, the maximum Bond number was $Bo = 5.6 \times 10^{-3}$. The experiment was controlled manually from the ground base.

In the initial configuration prior to the launch, the compensation tube and the nozzle were closed by the gate valve and the stemple. Once under microgravity conditions ($t' = 77$ s), the gate valve was opened and the compensation tube was filled by pu_1. Shortly after this, the stemple was removed from the nozzle and a capillary-driven flow into the test section ensued. After the contact with the suction head (outlet of the channel), the liquid was withdrawn by pu_2 and the system was ready for experiments ($t' = 115$ s).

Figure 6 shows the time-dependent run of the adjusted flow rates, Q' and Q'_s and the filling level H' of the compensation tube. During the experiment, the level H' rose continuously and had to be lowered six times. The experiment provides the options to change the flow rate in 0.46 ml s^{-1} or 0.04 ml s^{-1} increments. At first, a coarse approach to the critical flow condition with the larger increment was performed. For $Q' = 8.29$ ml s^{-1}, the flow became time dependent, indicated by the collapse of the surface ($t' = 195$ s). After that the step was repeated ($t' = 245$ s), but now leading to

https://doi.org/10.1017/S0022112004001041 Published online by Cambridge University Press

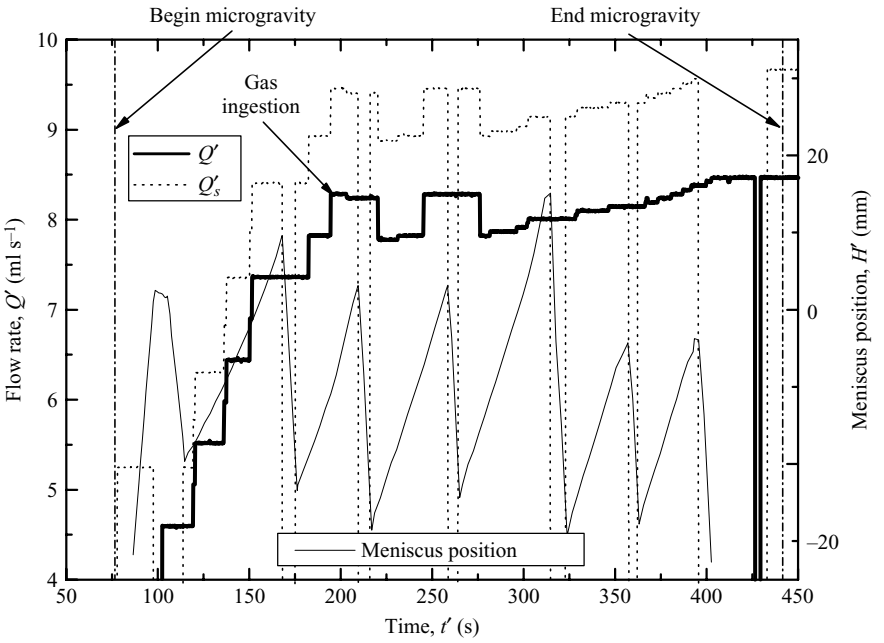


FIGURE 6. Adjusted flow rate Q' during the TEXUS-experiment. The liquid level H' inside the compensation tube rose continuously and had to be lowered six times by stopping the supplying flow rate Q'_s.

a steady flow. Then the flow rate was decreased for the approach to the critical flow rate with smaller step size. The maximum flow rate adjusted during this phase was $Q' = 8.38\,\mathrm{ml\,s^{-1}}$. Unfortunately, the microgravity time ended before the collapse of the surfaces occurred, thus the upper limit of flow rate was not achieved by the fine approach.

4.2. *Drop-tower experiments*

The experimental set-up consists of a circular container partly filled with test liquid and two parallel plates which are fixed upright on the container bottom. A suction device is mounted at the upper ends of the plates. By means of a piston, a constant flow rate can be withdrawn from the gap between the plates. Two CCD cameras are used for flow observation with the same perspective as in the TEXUS experiment shown in figure 5. The set-up is integrated into a drop capsule of the drop tower in Bremen. The section of the channel fills itself by capillary rise during the free fall of the capsule. When the liquid meniscus contacts the suction device, the piston is started with a constant volumetric flow rate Q. To determine the critical flow rate Q^{exp}_{crit}, several experiments at different flow rates must be performed. On average, 5 drops are used to determine Q^{exp}_{crit} with one experiment for reproduction.

Six different channels with two different liquids were investigated. The geometrical parameter, the liquid properties and the characteristic numbers of the experiments are provided in tables 3 and 4.

4.3. *Data evaluation*

The observations in both experiments are essentially the same. Typically, each stepwise change of the flow rate by ΔQ disturbs the flow and excites the liquid surfaces to

https://doi.org/10.1017/S0022112004001041 Published online by Cambridge University Press

oscillate. After a certain relaxation time, the disturbances are damped out and apart from slight oscillations the flow may be considered as steady if $Q < Q_{crit}$.

For comparison with the numerical data, both time-dependent profiles, k^L and k^R from figure 5(*b*), were analysed and averaged yielding the average profiles k. For this purpose the video material was digitized to 8 bit grey scale images. The profiles were detected using a 5×5 Sobel technique (Jaehne 1995) and corrected regarding the optical refraction at the interfaces of the glass plates. After consideration of errors due to ± 1 pixel resolution, the calibration and optical correction k is detected with an accuracy of approximately $\Delta k' = \pm 0.1$ mm.

The determination of S_{ca} from experiments is affected by the fact that the function $A(h)$ cannot be found from the experimental data. An approximate solution may be obtained, however, for small variation of A, assuming $d_x k \ll 1$. For this case, (2.13) reduces to $h = 1/R$, where R is defined in (2.16). In this approximation, the wave speed (3.2) and the speed index (3.3) yields

$$v_{ca1} = \frac{1}{R}\sqrt{A\frac{\mathrm{d}R}{\mathrm{d}A}}, \qquad S_{ca1} = QR\sqrt{\frac{1}{A^3}\frac{\mathrm{d}A}{\mathrm{d}R}\frac{\mathrm{d}R}{\mathrm{d}k}}. \tag{4.1}$$

The experimental critical flow rate Q_{crit}^{exp} is defined by

$$Q_{crit}^{exp} = \tfrac{1}{2}\left(Q_{max}^{st} + Q_{min}^{unst}\right), \tag{4.2}$$

where Q_{max}^{st} is the highest steady flow rate and Q_{min}^{unst} the lowest flow rate leading to the collapse of the free surface.

4.4. *Channel inlet boundary conditions*

Owing to the complex geometry, no analytical data for the determination of the boundary condition h_0 and s_0 from (2.19), (2.17) are available in sufficient accuracy and a direct measurement was not possible. For this reason, we performed three-dimensional model computations using the finite-element code FIDAP (Version 8.0, Fluent).

The capillary pressure at the channel inlet $h_0 = p_a - p_0$ is defined by the capillary pressure of the meniscus in the compensation tube $(p_a - p_1)$ plus convective and frictional flow losses inside the liquid reservoir and the nozzle (see figure 4). The pressure loss non-dimensionalized with $\rho'/2v_0^2$, $v_0 = v'(x = 0)$, is linear versus $1/Re_0$ with $Re_0 = 2av_0/\nu$ (White 1986). The regression of the numerical data yields the relation

$$h_0 = \frac{K_1 Q^2}{2} + \frac{K_2 Oh\, Q}{4} + K_3, \quad K_3 = \frac{a(p_a - p_1)}{2\sigma}. \tag{4.3}$$

The values of $K_{1,2,3}$ are given in table 5. Note that for the drop-tower experiments, the capillary pressure of the bulk surface is negligible compared to h_0 and therefore $K_3 = 0$.

To adapt the analytic entrance pressure loss proposed by Sparrow & Lin (1964) to the condition of the experiment, the velocity profiles at the channel inlet are compared between the three-dimensional model computations and the solution from Sparrow & Lin (1964), which gives values for s_0 in dependence of Q (compare with the end of § 2.2). It is remarkable that for all experimental configurations, s_0 is nearly a linear function of $1/Re_0$

$$s_0 = \frac{L}{Re_0} = \frac{LOh}{2Q}, \tag{4.4}$$

where the fitted values for L are given in table 5.

https://doi.org/10.1017/S0022112004001041 Published online by Cambridge University Press

Number	K_1	K_2	K_3	L	Q
TE-35a	1.4	374	0.222	−24	$0.44 < Q < 0.88$
DT-29	2.7	168	0	−5.5	$0.06 < Q < 0.40$
DT-32	2.2	91	0	−4.2	$0.07 < Q < 0.50$
DT-33	2.2	138	0	−6.6	$0.19 < Q < 0.57$
DT-34	2.3	215	0	−9.7	$0.19 < Q < 0.57$
DT-35/35a	2.0	180	0	−5.8	$0.44 < Q < 0.88$

TABLE 5. Coefficients for the entrance pressure drop at the inlet of the channel and for the velocity profile formula. The calculations have been performed with the flow rates indicated in the table to cover the region of the experimental data.

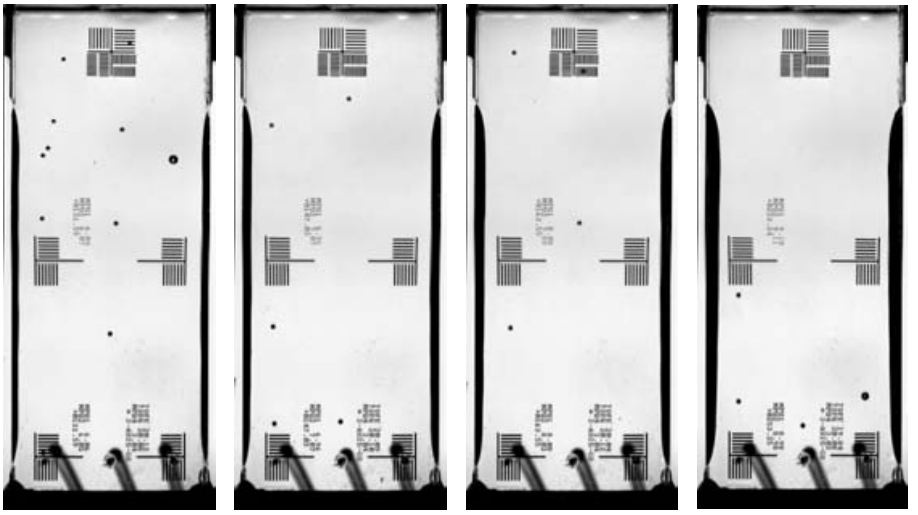


FIGURE 7. Steady flow in the open capillary channel at different flow rates below the critical value. The flow direction is from the bottom to the top. Owing to the decreasing pressure, the flow path narrows with increasing flow rate.

To obtain the best approximation to the one-dimensional model assumption, the flow path before the open channel of the TEXUS experiment was optimized. The model computations led to a nozzle with 25 mm by 30 mm rectangular inlet cross-section that converges to the channel cross-section. The nozzle has an elliptical shape in the (x, y)-plane, as shown in figure 4, but no constriction in the (x, z)-plane. With this form, the lateral velocity components in the entrance cross-section of the open channel were minimized to 2% of the longitudinal component. Concerning the x-component of the velocity, the flow is characterized by a constant core flow with small boundary layers along the walls.

5. Results and discussion

5.1. *Experimental observations*

Figure 7 shows the typical video images of the flow for $Q < Q_{crit}$ during the TEXUS experiment. As indicated by the dark zones, the surface profiles of the liquid are

https://doi.org/10.1017/S0022112004001041 Published online by Cambridge University Press

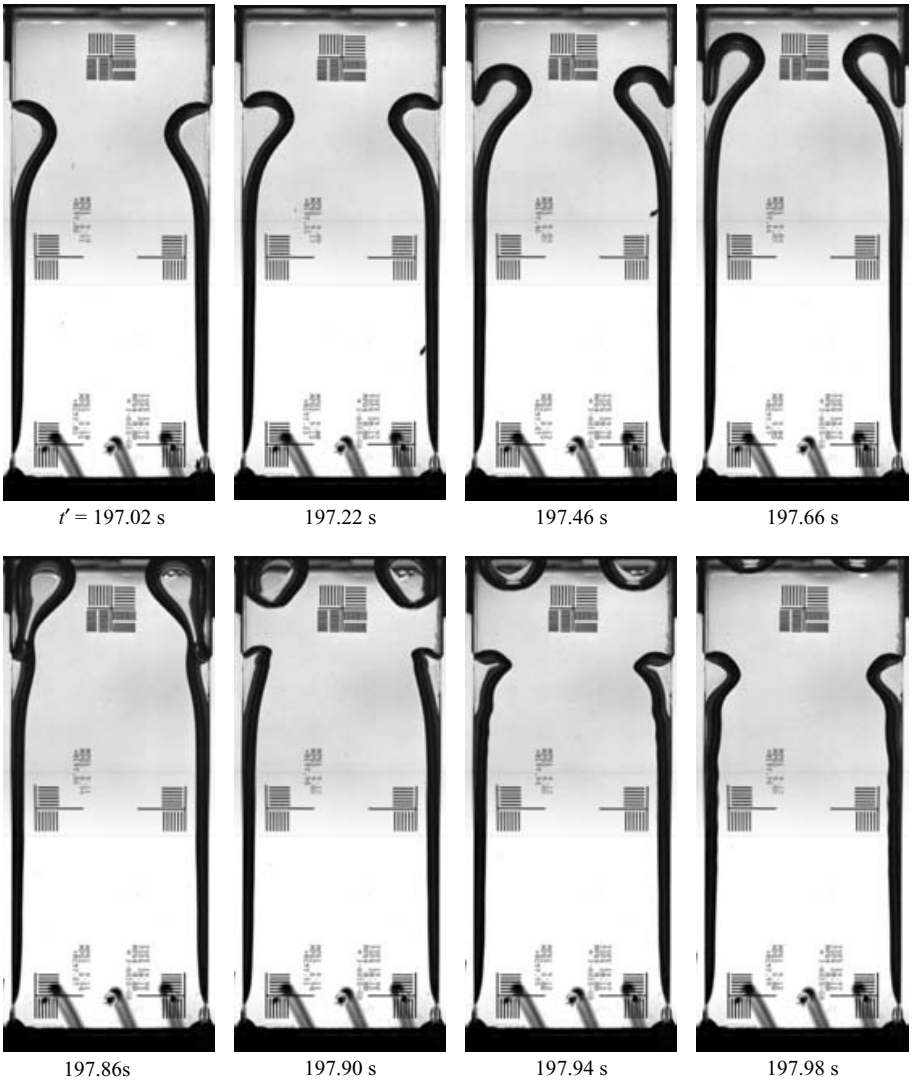


FIGURE 8. Unsteady liquid flow at a fixed flow rate above the critical value. The free surfaces collapse and a periodic ingestion of gas bubbles is observed.

symmetrical with respect to the plane $z = 0$. The cross-section of the flow path decreases in the flow direction and with increasing flow rate.

For $Q > Q_{crit}$, the surfaces collapse (figure 8). A periodic ingestion of gas bubbles is observed leading to a two-phase flow downstream the channel outlet. During the bubble formation, the surfaces stay pinned at the sidewalls of the outlet.

5.2. *Comparison of experimental and numerical profiles*

Figure 9(*a*) shows the average profile k along the channel axis x as a function of the adjusted flow rates Q for the TEXUS experiment. The labels refer to the evaluated sequences provided in table 6. For characterization, we introduce the lengths l_1 and l^*, where l_1 defines the inlet region with $1/R_2 > 0.01$, according to (2.13) and l^* the location of the smallest cross-section. With increasing flow rate, l^* decreases and the location of the minimum cross-section shifts towards the inlet. Along $0 \leqslant x \leqslant l_1$, the

https://doi.org/10.1017/S0022112004001041 Published online by Cambridge University Press

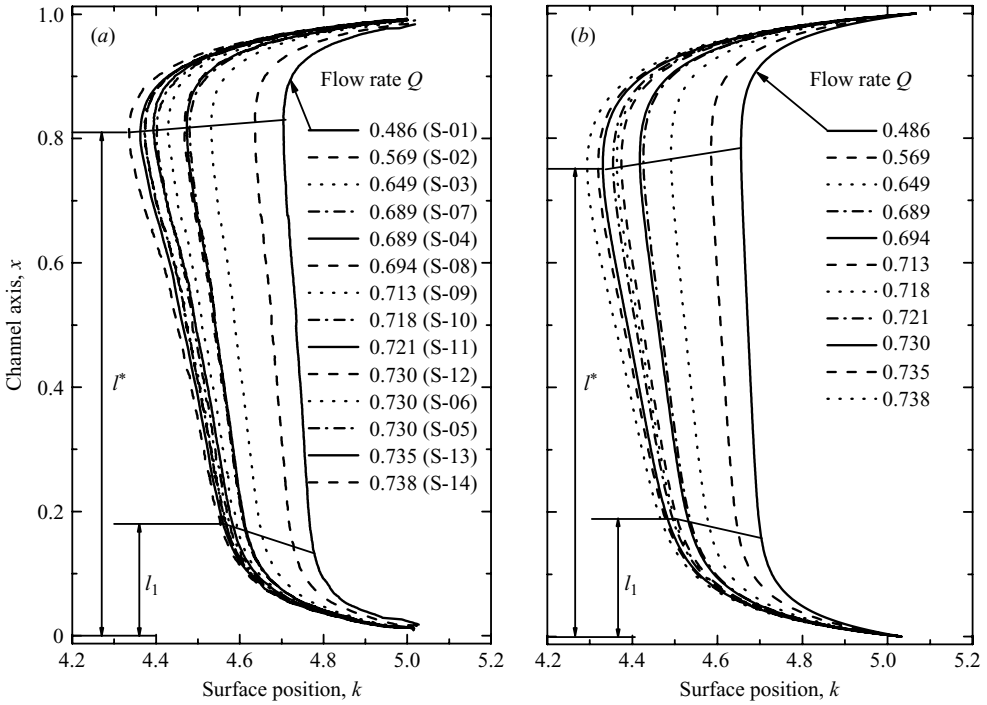


FIGURE 9. Profiles $k(x)$ of the TEXUS experiment versus the flow rate Q. (a) Experimental values, (b) numerical solution.

Number	t' (s^{-1})	Q' ($ml\,s^{-1}$)	Q	k^*	v^*	v^*_{ca1}	S^*_{ca1}
S-01	128.65	5.52	0.486	4.704 ± 0.036	0.506 ± 0.028	3.250 ± 0.131	0.16 ± 0.01
S-02	144.09	6.46	0.569	4.636 ± 0.036	0.598 ± 0.033	2.992 ± 0.144	0.20 ± 0.02
S-03	159.43	7.39	0.649	4.532 ± 0.036	0.694 ± 0.039	2.556 ± 0.154	0.27 ± 0.03
S-07	278.50	7.82	0.689	4.480 ± 0.036	0.743 ± 0.042	2.333 ± 0.154	0.32 ± 0.04
S-04	237.08	7.82	0.689	4.472 ± 0.036	0.745 ± 0.042	2.307 ± 0.154	0.32 ± 0.04
S-08	288.76	7.87	0.694	4.468 ± 0.036	0.750 ± 0.042	2.282 ± 0.154	0.33 ± 0.04
S-09	338.73	8.10	0.713	4.428 ± 0.036	0.776 ± 0.044	2.113 ± 0.153	0.37 ± 0.04
S-10	351.53	8.15	0.718	4.400 ± 0.036	0.785 ± 0.044	1.994 ± 0.152	0.39 ± 0.05
S-11	369.75	8.19	0.721	4.392 ± 0.036	0.789 ± 0.044	1.961 ± 0.152	0.40 ± 0.05
S-12	383.41	8.29	0.730	4.372 ± 0.036	0.802 ± 0.045	1.876 ± 0.151	0.43 ± 0.05
S-06	273.56	8.29	0.730	4.372 ± 0.036	0.802 ± 0.045	1.866 ± 0.151	0.43 ± 0.05
S-05	250.64	8.29	0.730	4.372 ± 0.036	0.802 ± 0.045	1.866 ± 0.151	0.43 ± 0.05
S-13	387.65	8.34	0.735	4.368 ± 0.036	0.808 ± 0.045	1.848 ± 0.151	0.44 ± 0.05
S-14	392.29	8.38	0.738	4.348 ± 0.036	0.815 ± 0.046	1.770 ± 0.150	0.46 ± 0.05

TABLE 6. Data from the TEXUS experiment: the flow rate Q, the average profile k, the average velocity $v = Q/A$, the wave speed v_{ca1} and the speed index S_{ca1}. Properties indicated by a star are determined at the minimum cross-section at $x = l^*$. t' denotes the beginning of the averaging interval.

curvature of the surfaces essentially adapts to the inlet pressure p_0 defined by h_0 from (4.3). Since $p_0 < p_a$ the surfaces bend inwards. The widening at the outlet is forced by the pinned surfaces at the sidewalls of the channel outlet. The labels in the figure indicate the chronological order in which the flow rates were adjusted during the

https://doi.org/10.1017/S0022112004001041 Published online by Cambridge University Press

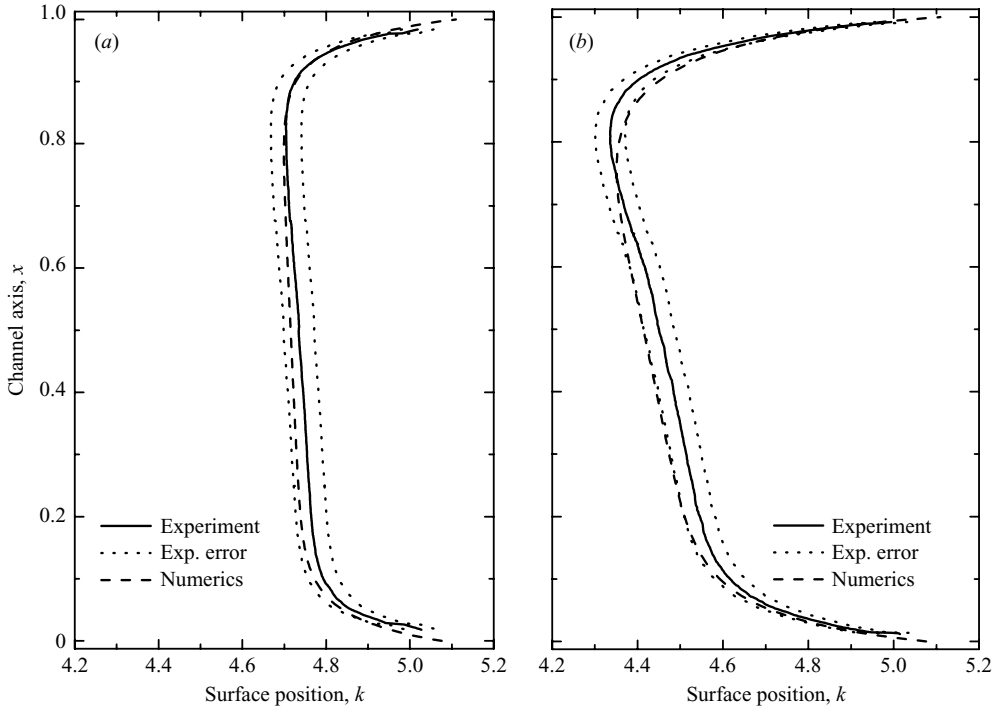


FIGURE 10. Evaluated profiles from the TEXUS experiment (solid lines), error of the profile data (dotted lines) and numerical prediction (dashed lines) for the lowest and the highest flow rate: (*a*) $Q = 0.486$ (S-01), (*b*) $Q = 0.738$ (S-14).

experiment. The comparison of the sequences S-04 and S-07 (both at $Q = 0.689$), as well as S-05, S-06 and S-12 (all at $Q = 0.730$) shows the high degree of reproducibility. The sequences S-05 and S-06 are evaluated before and after the compensation tube was emptied which illustrates the reproducibility of the pressure boundary condition inside the compensation tube. Note that because of insufficient contrast, the profile points near the inlet and outlet could not be detected. The solutions of (2.17) and (2.18) with the boundary conditions $\Lambda(x = 0) = 5.076$ and $\Lambda(x = 1) = 5.11$ (considering the metal plates from figure 5*a*) and (4.3), (4.4) are displayed in figure 9(*b*). The surface profiles for the different flow rates are in good agreement with the experimental data.

For a detailed comparison between experiment and theory, the lowest and the highest realized flow rates are depicted in figure 10. The experimental profiles (solid lines) are reproduced well by the numerical calculations (dashed lines). This level of agreement is achieved for all sequences given in table 6. All numerical profiles are located within the experimental error bars (dashed lines).

Figure 11 shows the average profiles of DT-29 and DT-35a representative for the drop-tower experiments given in table 7. These experiments differ in two aspects from the sounding rocket experiment: (i) The reorientation process of the liquid surface in the container does not decay during the brief experiment time which leads to disturbances of the inlet surface curvature h_0, and (ii) significant transverse flow components are also present since no nozzle is used to rectify the inlet flow. Nevertheless, the experimental profile data (solid line) and the numerical solution of (2.17) and (2.18) (dashed line) agree in several aspects. For small $\tilde{l}$, the profile minimum and the curvature at the outlet are predicted well by the computations, in

https://doi.org/10.1017/S0022112004001041 Published online by Cambridge University Press

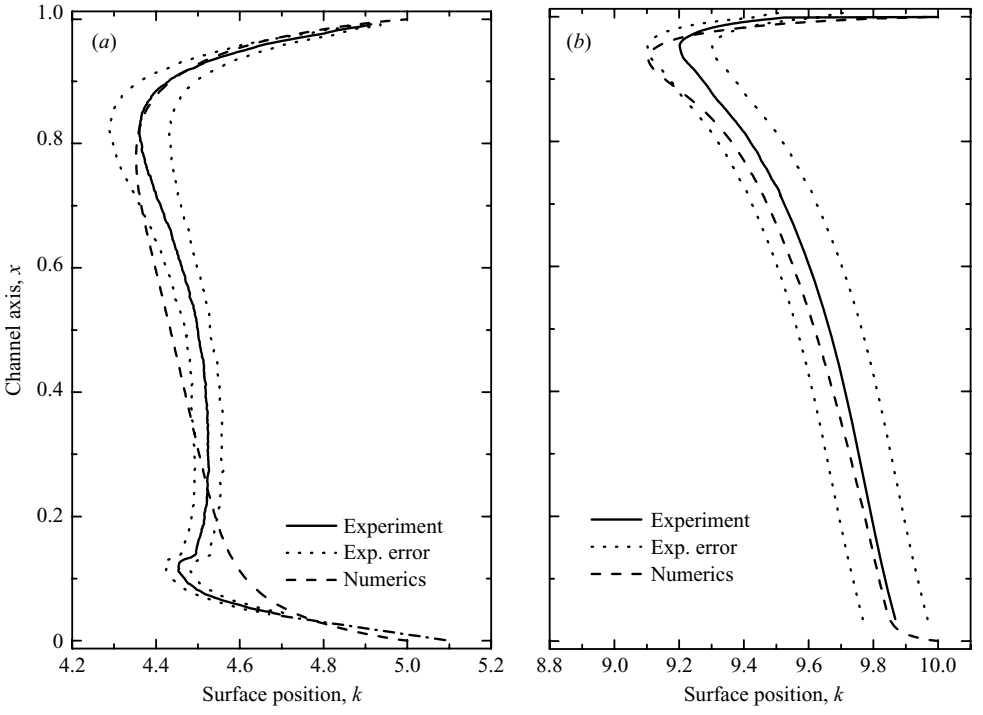


FIGURE 11. Evaluated profiles lines from the drop-tower experiments (solid lines), error of the profile data (dotted lines) and numerical prediction (dashed lines). (*a*) DT-35a, $Q = 0.771$, (*b*) DT-29, $Q = 0.38$. For the numerical calculation of DT-29 *Oh* was decreased by 2%, within the experimental error.

Number	Q^{st}_{max}	Q^{unst}_{min}	Q^{exp}_{crit}	Q^{num}_{crit}	k^*	S^{*exp}_{ca1}	S^{*num}_{ca}
TE-35a	0.738	–	–	0.776	4.35 ± 0.04	0.46 ± 0.05	0.43
DT-29	0.380	0.392	0.386 ± 0.006	0.391	9.05 ± 0.12	0.20 ± 0.07	0.23
DT-32	0.498	0.529	0.515 ± 0.017	0.588	2.95 ± 0.08	0.23 ± 0.03	0.25
DT-33	0.527	0.555	0.542 ± 0.015	0.603	9.38 ± 0.09	0.22 ± 0.05	0.23
DT-34	0.578	0.591	0.585 ± 0.007	0.616	9.38 ± 0.09	0.22 ± 0.05	0.24
DT-35	0.655	0.702	0.679 ± 0.024	0.730	4.49 ± 0.13	0.30 ± 0.07	0.29
DT-35a	0.771	0.796	0.784 ± 0.013	0.800	4.36 ± 0.07	0.47 ± 0.09	0.45

TABLE 7. Maximum steady flow rate Q^{st}_{max}, minimum unsteady flow rate Q^{unst}_{min}, experimental and numerical critical flow rate Q^{exp}_{crit} and Q^{num}_{crit}, minimum surface position k^*, experimental speed index in single radius approximation S^{*exp}_{ca1} and numerical with two radii of curvature S^{*num}_{ca} at the smallest cross-section for Q^{st}_{max} for all experiments.

contrast to long $\tilde{l}$, where the inflow region and the profile of the main flow path are in good agreement.

5.3. *The influence of the speed index and the maximum flow rate*

From (3.6), it is concluded that the maximum flow rate of the steady flow is reached when $S_{ca} = 1$ locally. To verify this, we calculated the S_{ca} from the experimental and numerical profiles k of the TEXUS experiment. The relevant location to consider S_{ca} follows from (3.10) and (3.11). Along $0 \leqslant x \leqslant l^*$, the flow requires positive gradients

https://doi.org/10.1017/S0022112004001041 Published online by Cambridge University Press

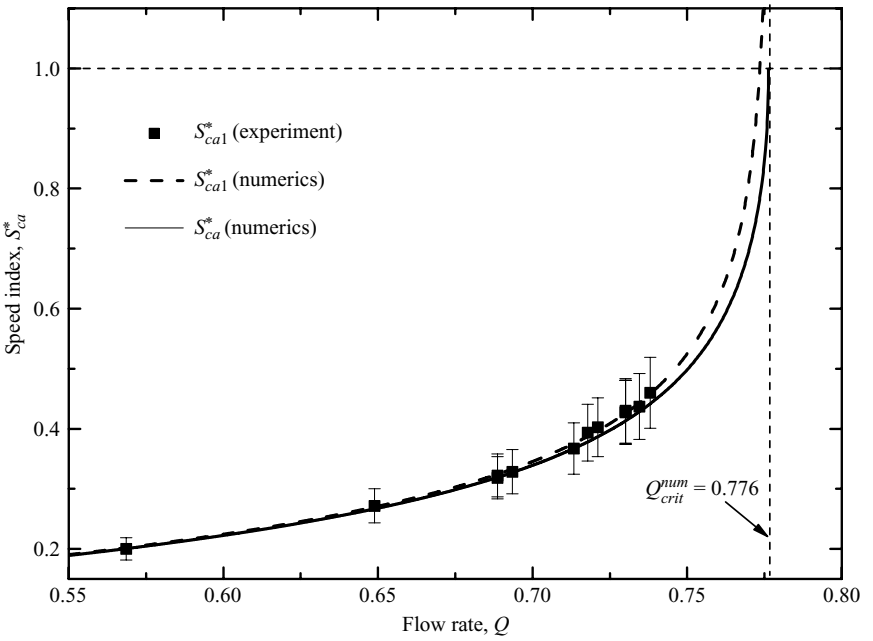


FIGURE 12. Speed index S^*_{ca} at the smallest cross-section of the flow as function of the adjusted flow rate Q for the TEXUS experiment: single radius approximation from the experiment (single squares with error bars) and the computations (dashed line), numerical data based on both radii of curvature R_1 and R_2 (solid line).

of h and negative gradients of A, thus $\mathrm{d}h/\mathrm{d}x > 0$ and $\mathrm{d}A/\mathrm{d}x < 0$. These gradients are only obtainable for $S_{ca} < 1$, from which we conclude that the investigated flow is subcritical. For subcritical flow, (3.11) states that the S_{ca} increases in the flow direction. Since (3.10) and (3.11) are monotonic functions, the maximum of S_{ca} appears at the smallest cross-section $A^* = A(x = l^*)$. For this location, table 6 provides the TEXUS data of S^*_{ca1} from (4.1) and the corresponding velocities, $v^* = Q/A^*$ and v^*_{ca1}. With increasing flow rate v^* increases for continuity reasons but v^*_{ca} decreases, thus S^*_{ca} increases. In figure 12 the experimental S^*_{ca1} and the numerical prediction of S^*_{ca1} and S^*_{ca} from (2.20) are plotted versus the flow rate. It shows that S_{ca} exactly tends towards unity for the numerical maximum flow rate $Q^{num}_{crit} = 0.776$. For $Q > 0.776$ no steady numerical solutions are possible. Owing to the good agreement of the experimental and theoretical profiles, the values of both S^*_{ca1} agree well. However, S^*_{ca1} is overestimated for $Q > 0.7$ because the radius of curvature in the flow direction, R_2, is not considered. Nevertheless, the experimental data follow the numerical trend of S^*_{ca} which confirms that the flow rate of the steady flow is limited owing to a choking effect.

From table 7, it follows that experimental steady flows were possible for $Q \lesssim 0.95 Q^{num}_{crit}$. A closer approach to the limit might be difficult from the experimental point of view since a small variation of Q leads to a large variation of S_{ca}. The final 5% of flow rate changes S^*_{ca1} by 50%. Close to the limit, very small increments in Q are required to increase the flow in quasi-static manner avoiding strong non-steady effects. For this reason, the collapse of the free surface was observed for $Q = 0.73$ ($t' = 195$ s) during the first increase of Q with the larger increments (see discussion in § 4.1.2).

https://doi.org/10.1017/S0022112004001041 Published online by Cambridge University Press

Owing to the short experiment time and the limited number of experiments, the flow-rate-dependent investigation of the speed index was not possible in the drop-tower experiments. However, the available data for Q_{crit}^{exp} in table 7 show a good agreement with the numerical predictions.

Although the formulation of the flow problem is steady, the longitudinal wave speed which appears in the momentum equation allows the following interpretation. To increase the flow rate, the pressure at the channel outlet must be decreased in response to an increase of the withdrawal pump flow rate. The local pressure disturbance generated at the pump propagates upstream, changes the pressure distribution $p(x)$ along the channel axis and establishes a higher flow rate. Inside the suction pipe, the disturbance travels at the speed of sound. Along the open channel, it propagates at the wave speed v_{ca} relative to the liquid flow. The relative velocity v_{rel} is given by

$$v_{rel} = v - v_{ca} = v_{ca}(S_{ca} - 1). \tag{5.1}$$

In the case of choking, S_{ca} becomes unity at $x = l^*$ and v_{rel} vanishes. For this reason, the pressure disturbance cannot pass the minimum cross-section and the distribution $p(x)$ remains unchanged along the flow path $0 \leqslant x \leqslant l^*$. To satisfy continuity, gas has to be ingested from the sides into the outlet. Thus, the free surfaces collapse and the flow becomes unsteady.

5.4. *Influence of the length $\tilde{l}$ on the profile formation and the speed index S_{ca}*

In § 3, the mechanism of choking based on an interaction between the pressure gradient and convective acceleration was discussed. Considering a subcritical flow, each increase of pressure gradient accelerates the liquid as long as the local liquid velocity is below the wave speed (3.1). Inspection of (2.4) and (2.17) shows that the pressure gradient is changed by the convective momentum transport $v\,\mathrm{d}v$ as well as by the frictional losses $\mathrm{d}w_f$. Depending on the dimensionless length $\tilde{l}$, two distinct cases may be identified. For sufficiently small $\tilde{l}$ the frictional pressure loss vanishes and choking is essentially caused by the convective term. In the opposite case, for sufficiently large $\tilde{l}$ the pressure gradient is only related to the irreversible frictional losses.

To investigate the influence of $\tilde{l}$ on the solution of (2.17), (2.18), we performed a parametric study. For each $\tilde{l}$ the maximum flow rate Q_{crit}^{num} and the corresponding mean curvature difference between the channel inlet and outlet, $\Delta h = h(x=1) - h(x=0)$, were determined. Since the reversible convective momentum transport does not affect a net decrease of pressure between the inlet and outlet, Δh is a direct measure for the influence of the frictional pressure loss. The calculations were performed for $s_0 > l_e$, assuming a fully developed parabolic velocity profile along the channel. The inlet pressure boundary condition h_0 was taken from the formula (4.3) with the coefficients $K_1 = 1.4$, $K_2 = 374$ and $K_3 = 0$. Figure 13 shows a plot for Δh as a function of $\tilde{l}$. The curve was computed for $Oh = 10^{-4}$ and $\Lambda = 5$, but can be seen to represent the general behaviour. The labels of the single squares refer to the experiments given in table 4 (black squares) and the two numerical cases discussed below (white squares). Note that owing to the different values of Λ and Oh, the experimental values of Δh deviate slightly from those given in figure 13 (deviation stays within the squares). The curve may be divided into three regions. For small flow lengths, ($\tilde{l} < 10^{-3}$), the irreversible pressure loss Δh is small and the flow is dominated by convective momentum transport. In the limit of a very short length, the curvature difference Δh tends to zero. For that case, the pressure loss along the flow path is fully reversible. For the other extreme of a very long channel, ($\tilde{l} \geqslant 10^{-1}$), the flow is dominated by

https://doi.org/10.1017/S0022112004001041 Published online by Cambridge University Press

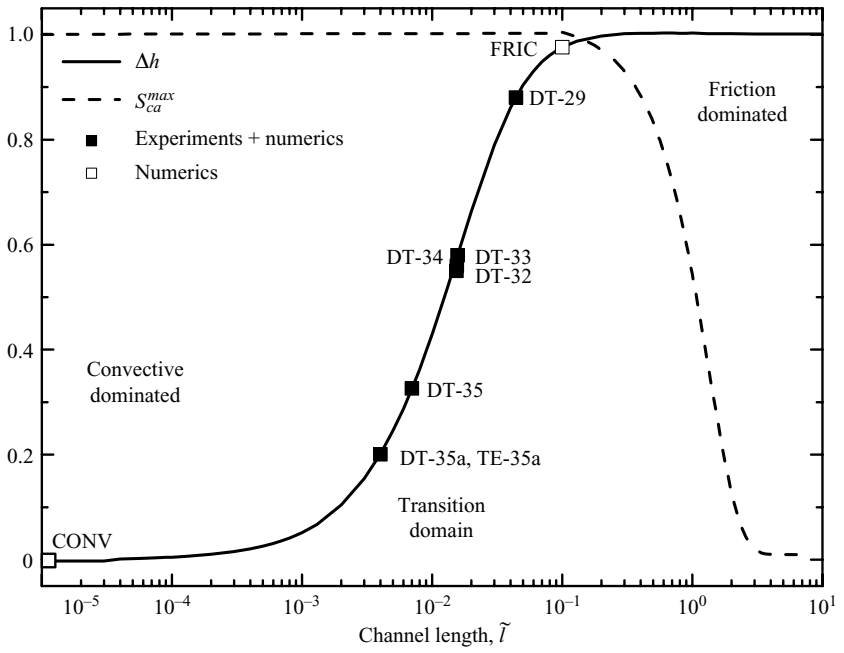


FIGURE 13. Irreversible pressure loss Δh as function of the channel length $\tilde{l}$ at Q_{crit}^{num}. The black squares are the experiments (see §4), the white squares the numerical examples, discussed in this section. The dashed line is the maximum speed index.

viscous momentum transport (convection contributes <1%). In the limit $\tilde{l} \to \infty$, the curvature difference Δh tends towards unity yielding a pure Stokes flow. Between these two extremes, denoted as the transition domain, the flow is controlled by both convective and frictional pressure losses. The influence of the domains on the nature of the flow is demonstrated by the numerical examples CONV ($Oh = 10^{-5}$, $\Lambda = 5$, $\tilde{l} = 10^{-5}$, $Q_{crit}^{num} = 1.123$) and FRIC ($Oh = 10^{-3}$, $\Lambda = 5$, $\tilde{l} = 0.1$, $Q_{crit}^{num} = 0.1927$). For the first example the flow properties k, v and h at the maximum flow rate Q_{crit}^{num} are shown in figure 14(*a*). Since the pressure loss due to convective momentum transport is reversible, the minimum cross-section appears at half the channel length $l^* = l/2$. The pressure loss along $0 < x < l^*$ is recovered along the distance $l^* < x < 1$. With increasing $\tilde{l}$ the frictional loss Δh increases and the position of the minimal cross-section l^* moves towards the outlet. The influence of the convective term vanishes. In the extreme example FRIC (figure 14*b*) the local importance of the convective term is reduced to a small zone at $x = l^*$, leading to the distinct constriction of the flow path at the channel outlet. As a result, the total frictional loss increases approximately linearly with x as indicated by the nearly linear increase h. Figure 15 shows S_{ca}^* versus Q/Q_{crit}^{num} for both examples. Both S_{ca}^* tend towards unity at critical conditions, but the rate of change differs significantly. In contrast to CONV the S_{ca}^* from example FRIC stays low for a wide range of Q ($S_{ca}^* < 0.1$ for $Q < 0.9 Q_{crit}^{num}$), but increases strongly for $Q > 0.9 Q_{crit}^{num}$. This behaviour demonstrates the small influence of the convective acceleration which is (i) significantly restricted to a small zone at the smallest cross-section and (ii) appears only when the flow runs near the critical condition. The drop-tower experiments which cover a wide range of the transitional domain ($10^{-3} < \tilde{l} < 10^{-1}$) confirm these findings. The experiment DT-35a at the

https://doi.org/10.1017/S0022112004001041 Published online by Cambridge University Press

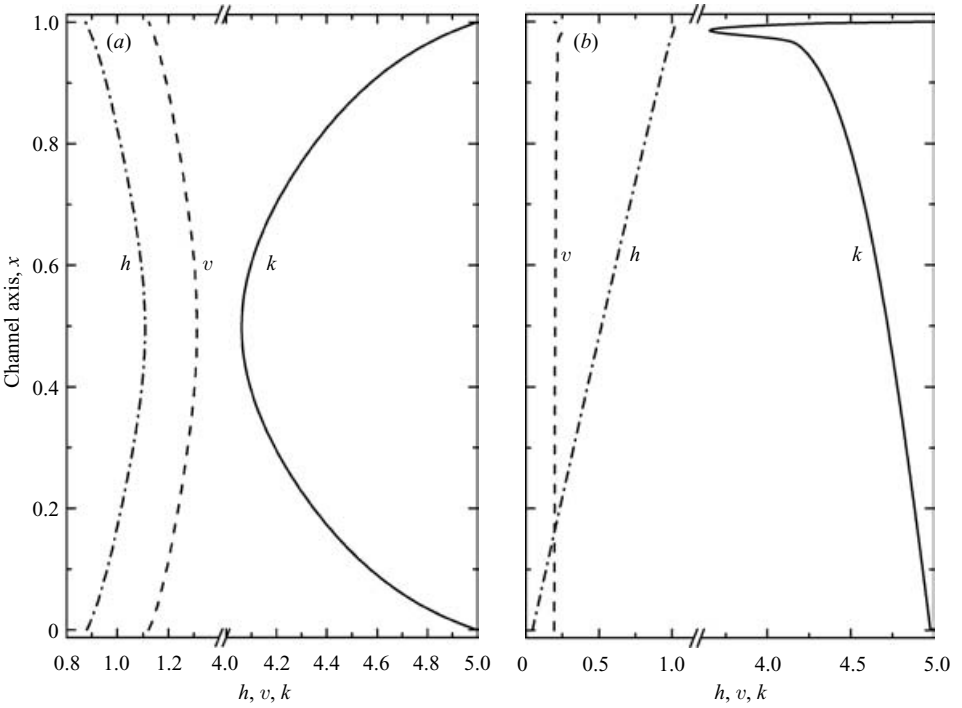


FIGURE 14. Numerical solutions for the profile k (solid line), the velocity v (dashed line) and the curvature h (dash-dot line) at Q_{crit}^{num}. (a) Example CONV, a typical flow dominated by convection. (b) Example FRIC, a typical flow dominated by friction.

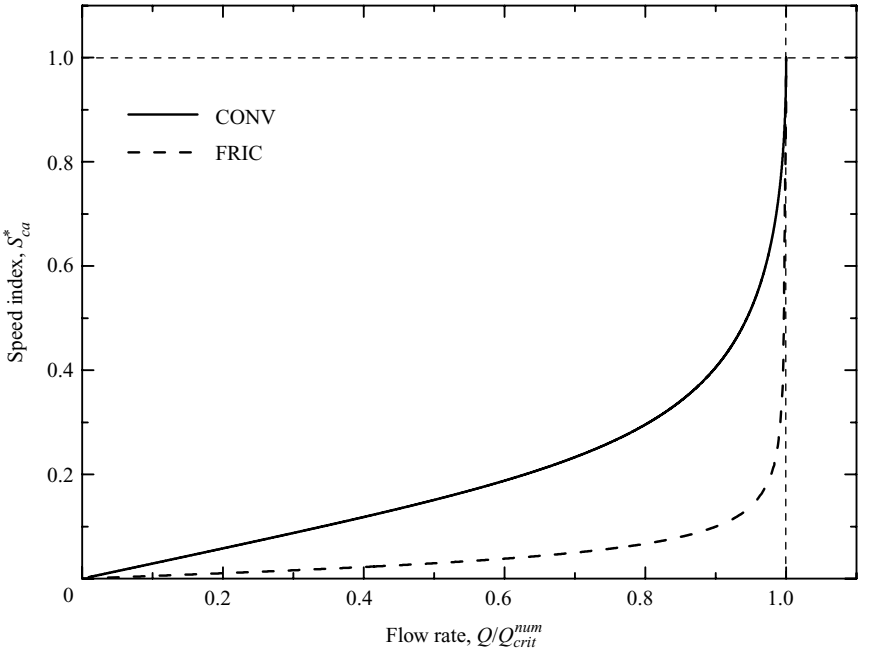


FIGURE 15. S_{ca}^* versus the flow rate Q/Q_{crit}^{num} for the two numerical examples CONV and FRIC.

https://doi.org/10.1017/S0022112004001041 Published online by Cambridge University Press

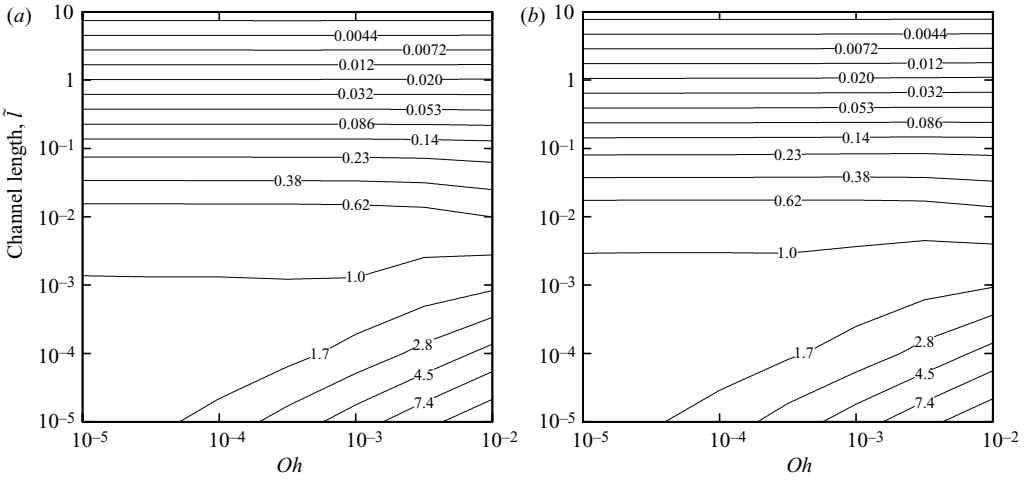


FIGURE 16. Contour maps of the critical flow rate Q_{crit}^{num} plotted in logarithmic scale as function of the Ohnesorge number and length $\tilde{l}$, (*a*) for $\Lambda = 5$ and (*b*) for $\Lambda = 50$.

lower range of the transitional domain is essentially dominated by the convective acceleration. Thus, the shape is similar to example CONV. Experiment DT-29 is dominated by friction characterized by the sharp distinct minimum of the cross-section as in the example FRIC.

For flow lengths $\tilde{l} > 0.1$, the flow variables do not deviate significantly from figure 14(*b*). However, the model computations state that the S_{ca} does not tend towards unity. As shown in figure 13, S_{ca}^{max} at Q_{crit}^{num} decreases rapidly and tends towards zero. Inasmuch as the choking effect depends on the interaction between the pressure gradient and the convective acceleration, the mechanism becomes insignificant if the convective term of (2.17) is negligibly small compared to the frictional term. In this situation, the flow is purely viscous limited. This limiting mechanism is akin to that of viscous flows in flexible tubes (Wilson, Rodarte & Butler 1986). For $\tilde{l} > 0.1$, $\Delta h = 1$ may be used to predict the maximum flow rate for friction dominated flow. With $\Delta h = 1$ and $\Lambda \to \infty$, integration of (2.17) neglecting the flow losses due the change of the velocity profile yields

$$Q_{crit} = \frac{2}{K_{pf}\tilde{l}}. \tag{5.2}$$

The knowledge of the maximum flow rate is important for technical applications. Figure 16 shows Q_{crit}^{num} for a wide range of the parameters ($10^{-5} \leqslant Oh \leqslant 10^{-2}$, $10^{-5} \leqslant \tilde{l} \leqslant 10$, $\Lambda = 5, 50$). Similar to the discussion of figure 13, three regions with a qualitatively different behaviour of Q_{crit}^{num} can be identified. As expected, the maximum flow rate decreases with increasing channel length. The maps indicate that the maximum flow rate is independent from Oh for friction-dominated flows ($\tilde{l} > 0.1$), which justifies that the Oh dependence is fully characterized by our dimensionless length $\tilde{l}$. In this region a fit of the data gives

$$Q_{crit} = \left(1 - \frac{1}{5\Lambda}\right) \frac{2}{K_{pf}\tilde{l}}, \tag{5.3}$$

which tends to (5.2) for $\Lambda \to \infty$. For smaller channel lengths, the maximum flow rate

https://doi.org/10.1017/S0022112004001041 Published online by Cambridge University Press

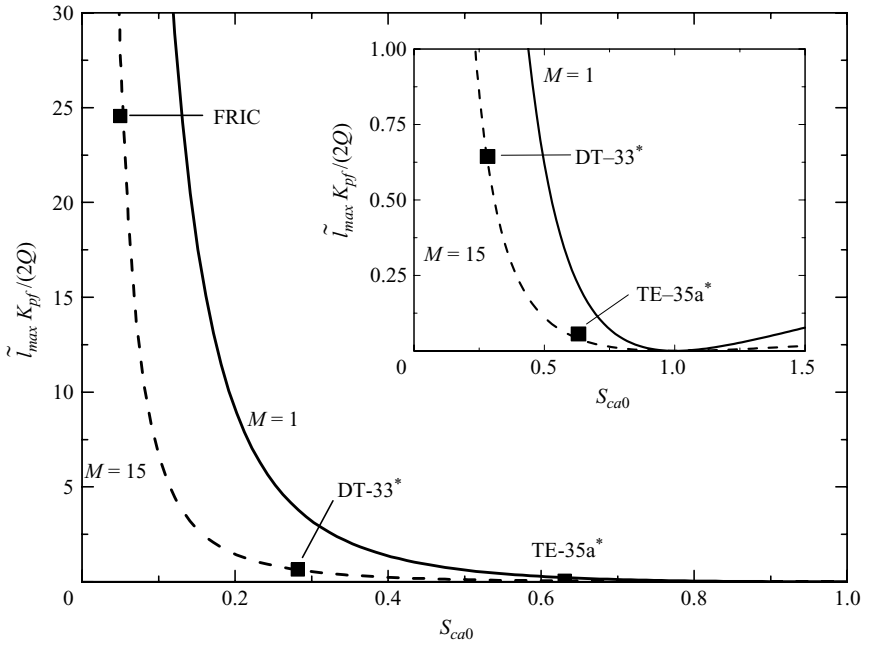


FIGURE 17. Analytical maximum channel length as a function of the inlet speed index S_{ca0} for $M = 1$ (solid line) and $M = 15$ (dashed line). For comparison, the examples FRIC, DT-33 and TE-35a are depicted. Note, that in contrast to the data in § 4, DT-33 and TE-35a were computed with $h_0 = 0.04$.

increases with increasing Oh in the convective flow domain. Similarly to the friction dominated regime, the values of Q_{crit}^{num} increase with increasing aspect ratio.

5.5. *Analytical solutions*

As a consequence of (3.11), we deduce an analytical solution for the maximum channel length at $S_{ca} = 1$. For simplification, a flow with a fully developed velocity profile and small curvature of the surface is assumed. With the latter assumption, $A(h)$ may be approximated linearly so that the definition of M in (3.8) yields $M = 1$. Numerical computations using the complete model show that M varies within the range of $1 \leqslant M \leqslant 70$. We now understand M as an average constant property. The integration of equation (3.9) from the channel inlet at $x = 0$ (with $A(x = 0) = 1$ and $S_{ca}(x = 0) = S_{ca0}$) to an arbitrary channel position x then yields $A = (S_{ca0}/S_{ca})^{2/(2+M)}$. With this expression, we obtain

$$\tilde{l}_{max} \frac{K_{pf}}{2Q} = 1 - \frac{M+2}{M+1} S_{ca0}^{-2/(M+2)} + \frac{1}{M+1} S_{ca0}^{-2} \tag{5.4}$$

by integration of (3.11) within the limits ($x = 0$, $S_{ca} = S_{ca0}$) and ($x = \tilde{l}_{max}$, $S_{ca} = 1$). Figure 17 shows the analytic solutions (5.4) for $M = 1$ (solid line) and $M = 15$ (dashed line). The black squares are numerical solutions of (2.17) and (2.18) performed for the parameters of FRIC, DT-33 and TE-35a with the boundary condition $h_0 = 0.04$. Obviously a constant M ($M = 15$ in the case of small h_0) is sufficient to obtain a good agreement between the analytical solution and the numerical computation for the complete transition flow regime addressed in figure 13.

https://doi.org/10.1017/S0022112004001041 Published online by Cambridge University Press

6. Summary

In this work, the forced liquid flow through an open capillary channel under low-gravity conditions was investigated experimentally, numerically and theoretically. Besides the determination of key characteristic features of the flow such as the profile lines of the surface shape and the critical flow rate, the investigations focused on the effect of flow rate limitation due to choking. Flow rate limitations are observed if the adjusted flow rate of the steady flow exceeds a certain limit leading to a collapse of the free surfaces at the outlet. Under such conditions, the governing steady-state equation yields no solution and the flow becomes unsteady.

The particular channel studied consists of two parallel plates with small uniform gap, bounded by free liquid surfaces at the open sides. A one-dimensional flow model is presented in which the liquid pressure is related to the capillary pressure at the free surface including both principal radii of curvature. Besides the convective and viscous losses, the flow model considers the additional pressure loss due to the change of the velocity profile in the entrance region. The gap ratio Λ, the Ohnesorge number Oh and the dimensionless length $\tilde{l}$ are identified as the governing parameters of the flow. The governing equations are solved numerically, yielding the maximum flow rate and the innermost surface position as a function of these parameters.

Owing to the form of the governing equations, similarities exist between the channel flows and compressible gas flows as well as open channel flows under normal gravity conditions. The longitudinal small-amplitude wave speed is responsible for the occurrence of choking and is discussed. By the ratio of the mean liquid velocity and the longitudinal wave speed a local capillary speed index is introduced. A reformulation of the momentum equation in terms of this speed index shows that the flow rate is limited if the local speed index becomes unity – the choking condition.

Experiments in a drop tower and aboard a sounding rocket are presented. The drop-tower experiments are designed to determine the surface profiles and the maximum flow rate as a function of Λ, Oh and $\tilde{l}$. Both data show good agreement with the numerical calculations. The influence of the speed index is studied aboard the sounding rocket for a single parameter set of the dimensionless numbers. During the ballistic flight, the flow rate is increased incrementally to the upper limit. To the favourable agreement of the experimental and numerical profiles, the speed index also agrees with the numerical prediction. Since it tends towards unity for increasing flow rate, we conclude that the collapse of the surface occurs because of the occurrence of choking.

Finally, a numerical parameter study is performed that identifies three regions in which the flow limitation is caused by convective and frictional pressure losses leading to distinctly different interface profiles, which correspond to the experimentally determined profiles. The limit of application of the choking model is shown which appears in the case of the Stokes flow approximation. For this friction-dominated case we find an expression for the maximum flow rate expressed in terms of the key parameters of the problem. Invoking several approximations, an analytic solution is possible yielding the maximum channel length for given inlet boundary conditions.

The funding of the drop-tower flights and the sounding rocket flight by the European Space Agency (ESA) and the funding of the research project by the German Federal Ministry of Education and Research (BMBF) through the German Aerospace Center (DLR) under grant numbers 50WM0241 and 50WM9901 are gratefully acknowledged. We wish to thank Mr P. Prengel for the experimental set-up,

https://doi.org/10.1017/S0022112004001041 Published online by Cambridge University Press

the TEXUS team and in particular Mr D. Grothe for the support and Dr E. Ramé for valuable comments.

REFERENCES

Bronstein, I. N. & Semendjajew, K. A. 2004 *Handbook of Mathematics*, 4th edn. Springer.

Dreyer, M. E., Delgado, A. & Rath, H. J. 1994 Capillary rise of liquid between parallel plates under microgravity. *J. Colloid Interface Sci.* **163**, 158–168.

Jaehne, B. 1995 *Digital Image Processing*. Springer.

Jaekle, Jr., D. E. 1991 Propellant management device conceptual design and analysis: vanes. *AIAA Paper* 91-2172, pp. 1–13.

Landau, L. D. & Lifschitz, E. M. 1959 *Fluid Mechanics, Course of Theoretical Physics*, vol. 6. Pergamon.

Lighthill, J. 1978 *Waves in Fluids*, 3rd edn. Cambridge University Press.

Press, W. H., Teukolsky, S. A., Vetterling, W. T. & Flannery, B. P. 1992 *Numerical Recipes in C*. Cambridge University Press.

Rosendahl, U., Ohlhoff, A., Dreyer, M. E. & Rath, H. J. 2002 Investigation of forced liquid flows in open capillary channels. *Microgravity Sci. Technol.* **13**, 53–59.

Shapiro, A. H. 1953 *The Dynamics and Thermodynamics of Compressible Fluid Flow, vol. II*. Ronald Press.

Shapiro, A. H. 1977 Steady flow in collapsible tubes. *Trans. ASME: J. Biomech. Engng* **99**, 126–147.

Sparrow, E. M. & Lin, S. H. 1964 Flow development in the hydrodynamic entrance region of tubes and ducts. *Phys. Fluids* **7**, 338–347.

Srinivasan, R. 2003 Estimating zero-*g* flow rates in open channels having capillary pumped vanes. *Intl J. Numer. Meth. Fluids* **41**, 389–417.

White, F. 1986 *Fluid Mechanics*. McGraw-Hill.

Wilson, T. A., Rodarte, J. R. & Butler, J. P. 1986 *Wave-speed and viscous flow limitation, Handbook of Physiology*, Sec. 3, Part 1, pp. 55–61. American Physiological Society.

https://doi.org/10.1017/S0022112004001041 Published online by Cambridge University Press